

Ocean Chlorofluorocarbon and Heat Uptake during the Twentieth Century in the CCSM3

PETER R. GENT, FRANK O. BRYAN, GOKHAN DANABASOGLU, AND KEITH LINDSAY

National Center for Atmospheric Research, Boulder, Colorado*

DAISUKE TSUMUNE

Central Research Institute of Electric Power Industry, Chiba, Japan

MATTHEW W. HECHT

Los Alamos National Laboratory, Los Alamos, New Mexico

SCOTT C. DONEY

Woods Hole Oceanographic Institution, Woods Hole, Massachusetts

(Manuscript received 26 January 2005, in final form 22 August 2005)

ABSTRACT

An ensemble of nine simulations for the climate of the twentieth century has been run using the Community Climate System Model version 3 (CCSM3). Three of these runs also simulate the uptake of chlorofluorocarbon-11 (CFC-11) into the ocean using the protocol from the Ocean Carbon Model Intercomparison Project (OCMIP). Comparison with ocean observations taken between 1980 and 2000 shows that the global CFC-11 uptake is simulated very well. However, there are regional biases, and these are used to identify where too much deep-water formation is occurring in the CCSM3. The differences between the three runs simulating CFC-11 uptake are also briefly documented.

The variability in ocean heat content in the 1870 control runs is shown to be only a little smaller than estimates using ocean observations. The ocean heat uptake between 1957 and 1996 in the ensemble is compared to the recent observational estimates of the secular trend. The trend in ocean heat uptake is considerably larger than the natural variability in the 1870 control runs. The heat uptake down to 300 m between 1957 and 1996 varies by a factor of 2 across the ensemble. Some possible reasons for this large spread are discussed. There is much less spread in the heat uptake down to 3 km. On average, the CCSM3 twentieth-century ensemble runs take up 25% more heat than the recent estimate from ocean observations. Possible explanations for this are that the model heat uptake is calculated over the whole ocean, and not just in the regions where there are many observations and that there is no parameterization of the indirect effects of aerosols in CCSM3.

1. Introduction

What is required of a good ocean component for climate models? The first requirement is that the model

produce a realistic sea surface temperature (SST) distribution, given accurate atmospheric forcing. This is necessary if the model's climate is to be realistic and stable. However, another very important requirement is to get the rate of ocean heat uptake correct. This is the primary way in which the ocean affects the transient climate response of the fully coupled model, see Raper et al. (2002). A third requirement is to get the correct rate of ocean carbon dioxide uptake because this affects the amount of carbon dioxide that remains in the atmosphere. These requirements necessitate a very good representation of ocean mixed layer depths, ventilation

* The National Center for Atmospheric Research is sponsored by the National Science Foundation.

Corresponding author address: Dr. Peter Gent, NCAR, P.O. Box 3000, Boulder, CO 80307.
E-mail: gent@ucar.edu

of the main thermocline, and the global meridional overturning circulation (MOC), see Doney et al. (2004).

One method of assessing an ocean component is to evaluate the ventilation rate of the thermocline and deep ocean in simulations of the twentieth century. An ensemble of nine of these simulations from 1870–2000 has been made with the Community Climate System Model version 3 (CCSM3). These simulations use the best estimates of solar, aerosol and greenhouse gas forcing variations over the twentieth century, which are documented in Meehl et al. (2006). To validate CCSM3, results from the ocean component can be compared to ocean observations from the second half of the twentieth century. Three members of the ensemble, and an ocean-alone simulation forced by atmospheric observations, include chlorofluorocarbon-11 (CFC-11) as a passive tracer.

CFC-11 started to be released into the atmosphere in the 1930s. However, significant concentrations in the atmosphere and ocean did not occur until the 1950s. A large number of CFC observations were made during the World Ocean Circulation Experiment (WOCE) in all basins, concentrated in the 1991–97 period. Enough observations have been made that global, gridded datasets are now available, along with a total ocean inventory for 1991–97, see Willey et al. (2004). CFC-11 is a purely passive ocean tracer and is extremely useful in evaluating thermocline ventilation rates and deep-water formation sites in ocean models. In fact, the Ocean Carbon Model Intercomparison Project (OCMIP) specifically used CFC-11 to intercompare 13 global ocean models, see Dutay et al. (2002). Many of these were used as components of climate models, including the low resolution ocean component of the Climate System Model version 1 (CSM1). The CSM1 results from an ocean-alone run forced by atmospheric observations are discussed much more fully in Doney and Hecht (2002). They showed a large sensitivity of Antarctic Bottom Water formation to the surface forcing used and how incorporation of ocean physical parameterizations, such as a bottom boundary layer scheme, can improve the deep ocean uptake of CFC-11 around Antarctica. CFC-11 was not included in any CSM1 or CCSM version 2 (CCSM2) coupled runs, so this type of evaluation of the CCSM3 is new.

Ocean heat uptake in the entire ensemble will also be studied. We will compare the magnitude of long-term secular trends in heat content relative to the internal variability of the coupled model. Levitus et al. (2000) estimated long-term secular trends in ocean heat content from observations and showed that the ocean had taken up heat between the 1950s and 1990s, with a

significant increase in the average temperature of the upper 300 m. Several climate groups have analyzed their twentieth-century runs to compare with these observations, and all have concluded that there is only a small probability that the increase is due to natural variability. Gent and Danabasoglu (2004) analyzed control and 1% per year increasing carbon dioxide coupled runs using the CCSM2, and reached the same conclusion. We will compare ocean heat uptake results from the ensemble of CCSM3 twentieth-century runs to the recently updated Levitus et al. (2005) estimates and make inferences about the model internal variability and climate sensitivity.

The layout of the paper is as follows. The ocean and sea ice components and the CCSM3 coupled experiments will be briefly documented in section 2. The comparisons of CFC-11 and heat uptake with ocean observations are in sections 3 and 4, respectively. Section 5 contains our discussion and conclusions.

2. The ocean and sea ice components and experiments

The ocean component uses spherical coordinates in the Southern Hemisphere, but in the Northern Hemisphere the pole is displaced into Greenland at 80°N, 40°W. The horizontal grid has 320 (zonal) \times 384 (meridional) grid points, and the resolution is uniform in the zonal, but not in the meridional, direction. In the Southern Hemisphere, the meridional resolution is 0.27° at the equator, gradually increasing to 0.54° at 33°S, and is constant at higher latitudes. There are 40 levels in the vertical, whose thickness increases from 10 m near the surface to 250 m in the deep ocean. The minimum and maximum depths are 30 m and 5.5 km. The domain is global, which includes Hudson Bay, the Mediterranean Sea, and the Persian Gulf. The time step used is 1 h, which is small enough that no Fourier filtering is required around the displaced Greenland pole.

The horizontal viscosity is a Laplacian operator that is anisotropic, following the formulation of Smith and McWilliams (2003), and uses different coefficients in the east–west and north–south directions. The vertical mixing scheme is the *K*-profile parameterization (KPP) scheme of Large et al. (1994). A change in the KPP numerical implementation, compared to the CCSM2, has resulted in deeper, more realistic ocean mixed layer depths. The parameterization of the effects of meso-scale eddies is that of Gent and McWilliams (1990). The sea surface height is variable, but the ocean has a constant volume, which means that the freshwater flux is converted into an implied salt flux using a constant reference salinity. Further documentation of the CCSM3

TABLE 1. List of numerical experiments.

Label	Description	Run years	CFCs
NC1870	1870 control	280–510	
NCa	Twentieth century	360–490	
ORb	Twentieth century	380–510	
NCc	Twentieth century	400–530	
ORd	Twentieth century	420–550	
NCe	Twentieth century	440–570	
ES1870	1870 control	300–960	
ESb	Twentieth century	380–510	Yes
ESf	Twentieth century	410–540	
ESg	Twentieth century	460–590	Yes
ESh	Twentieth century	540–670	Yes
Ocn	Ocean alone	1958–2000	Yes

ocean component can be found in Danabasoglu et al. (2006) and Smith and Gent (2004).

The CCSM3 sea ice component is a dynamic, thermodynamic model that uses the elastic–viscous–plastic rheology of Hunke and Dukowicz (1997) and the Bitz et al. (2001) ice thickness distribution. This gives realistic simulations of sea ice concentration in CCSM3 coupled integrations, and the implied salt flux into the ocean is calculated from ice conditions including melting or freezing.

The implementation of the CFCs follows the OCMIP-2 protocols, see section 3 of Dutay et al. (2002), except that surface wind speed, atmospheric pressure, and ice fraction are from the atmosphere and sea ice components, and not from the specified protocols. In particular, where sea ice occurs the CFC ocean flux is multiplied by one minus the sea ice fraction. However, there was an error in the implementation of the transition between the Northern and Southern Hemisphere atmospheric CFC partial pressure (pCFC). The transition was imposed over ± 10 radians instead of $\pm 10^\circ$ so that most of the ocean saw near-equatorial values of atmospheric pCFC. The hemispheric pCFC averages should differ by 10%–20%, with the Northern Hemisphere having the larger values. This is a result of the larger Northern Hemisphere sources and a not very fast interhemispheric mixing time. Thus, while the model hemispheric oceanic CFC inventories are biased by 5%–10%, the error in the global oceanic CFC inventories is much smaller because the two hemispheric biases compensate each other quite closely. The implementation was correct in the CCSM3 ocean-alone run forced by observations.

A list of all integrations is shown in Table 1. The final configuration of the 1870 control (NC1870) integration was run at the National Center for Atmospheric Research (NCAR) for years 280–510. Five twentieth-century integrations were run at NCAR and Oak Ridge

National Laboratory, that branched from the NC1870 run at years 360, 380, 400, 420, and 440, respectively, and run for 130 years; 1870–2000. These are labeled NCa, ORb, NCc, ORd, and NCe in Table 1. Another 1870 control integration was run at the Earth Simulator (ES1870), which branched from the NC1870 run at year 300 and continued until year 960. Four twentieth-century integrations were run at the Earth Simulator, labeled ESb, ESf, ESg, and ESh, that branched from the ES1870 run at years 380, 410, 460, and 540, respectively. Runs ESb, ESg, and ESh are the three twentieth-century integrations that contain simulations of CFC-11. In addition to these fully coupled runs, we show results from a CCSM3 ocean-alone integration for the time period 1958–2000, labeled Ocn in Table 1. This run was forced by observed atmospheric fields and sea ice concentration that are documented in Large and Yeager (2004). The implied salt flux into the ocean under ice is a monthly mean climatology taken from an earlier coupled ocean and sea ice integration that was forced by atmospheric observations.

3. CFC-11 results

First, qualitative comparisons with CFC-11 observations taken on particular WOCE sections in the North and South Atlantic and South Pacific will be made. These sections were chosen because they include regions where there is significant ventilation of the deep ocean. In other regions, such as the Indian and North Pacific Oceans where most of the CFC-11 has remained in the upper ocean, comparisons between the model and WOCE sections are good. This indicates that the KPP vertical mixing scheme and wind-driven thermocline ventilation are performing quite well. CFC solubility is a strong function of temperature, so the data–model comparison of CFC-11 concentrations will reflect both the temperature structure and ventilation pathways of the ocean. An alternative approach is to compare CFC partial pressures, but we will not do this here.

Figure 1a shows the monthly averaged CFC-11 from NA93, the August 1993 NOAA reoccupation of the WOCE A16N section along 20°W in the North Atlantic. Figures 1b and 1c show the comparable plots from the Ocn run and the mean of the ESb, ESg, and ESh runs. The observations show most of the CFC-11 above 500 m in the subtropics, with surface values of about 2 pmol kg^{-1} . The surface value increases monotonically toward higher latitudes and attains a value of about 4 pmol kg^{-1} at 62°N . The CFC has also penetrated deeper monotonically toward the north, with the 0.1 pmol kg^{-1} contour reaching 4-km depth by 50°N . Pole-

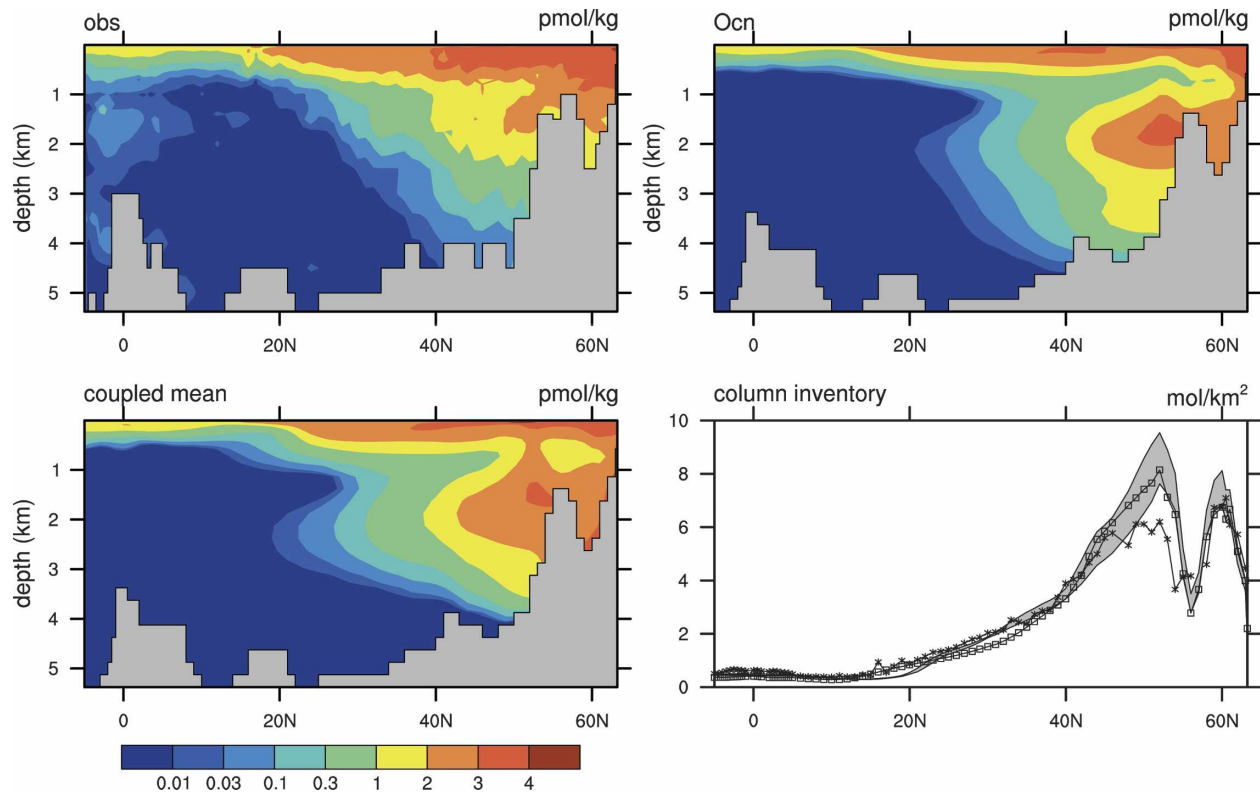


FIG. 1. CFC-11 from the NA93 section along 20°W taken in August 1993: (a) Observations, (b) ocean-alone Ocn run, (c) mean of the ESb, ESg, and ESh runs, and (d) column inventory of CFC-11 in moles km^{-2} along the section from observations (crosses), Ocn run (squares), and the range of the ESb, ESg, and ESh runs (shading).

ward of 45°N, the 1 pmol kg^{-1} value is at a depth of about 2 km. The ocean-alone and coupled runs show the same general features, but there are important differences. They have too small values between 600 m and 1 km north of 45°N, and too large values between 1.5 and 2 km centered at 50°N. The error between 600 m and 1 km is probably a result of the model Gulf Stream directly bringing low CFC-11 water from the south into this region because it is too zonal across the North Atlantic. The high values below suggest that high CFC water is being advected east of the Mid-Atlantic Ridge from the western North Atlantic instead of moving more directly southward as part of the deep western boundary current. The low CFC values in the model deep western boundary current likely cause the model to miss the higher values observed in the deep ocean along the equator, which are shown in Fig. 1a. The ensemble spread across the three CFC runs is shown in Fig. 1d. This shows the column inventory along the section from the observations (crosses), Ocn run (squares), and the shading gives the range from the ESb, ESg, and ESh runs. There is very little spread south of 40°N, but considerable spread farther north around 50°N. This is caused by the different timing of deep mixing events,

centered at 50°N, that penetrate through the CFC minimum at 1 km. Even so, the ensemble spread does not bracket the observations at this latitude.

Figure 2 shows the equivalent plot for the AJAX section along 0° in the South Atlantic from October 1983. The observations show high values $>1 \text{ pmol kg}^{-1}$ reaching down to 800 m in a region centered at 40°–45°S. This represents subduction of surface water down along isopycnal surfaces. There are values $>0.1 \text{ pmol kg}^{-1}$ throughout the water column between 53° and 60°S, which is only reproduced very weakly in the Ocn run, but is much better in the twentieth-century runs. This is probably due to stronger winds in the coupled runs, especially between 40° and 50°S. The Ocn run has a poor representation of the deep ocean observations, which is only improved somewhat in the coupled runs. Doney and Hecht (2002) show a similar poor representation of the deep observations along this section using the CSM1 ocean component. They traced this to insufficient westward transport of deep CFC-tagged water along the continental slope of Antarctica east of the Weddell Sea. The comparison between model results and observations was better a little farther west directly north of the Weddell Sea. Figure 2d shows the en-

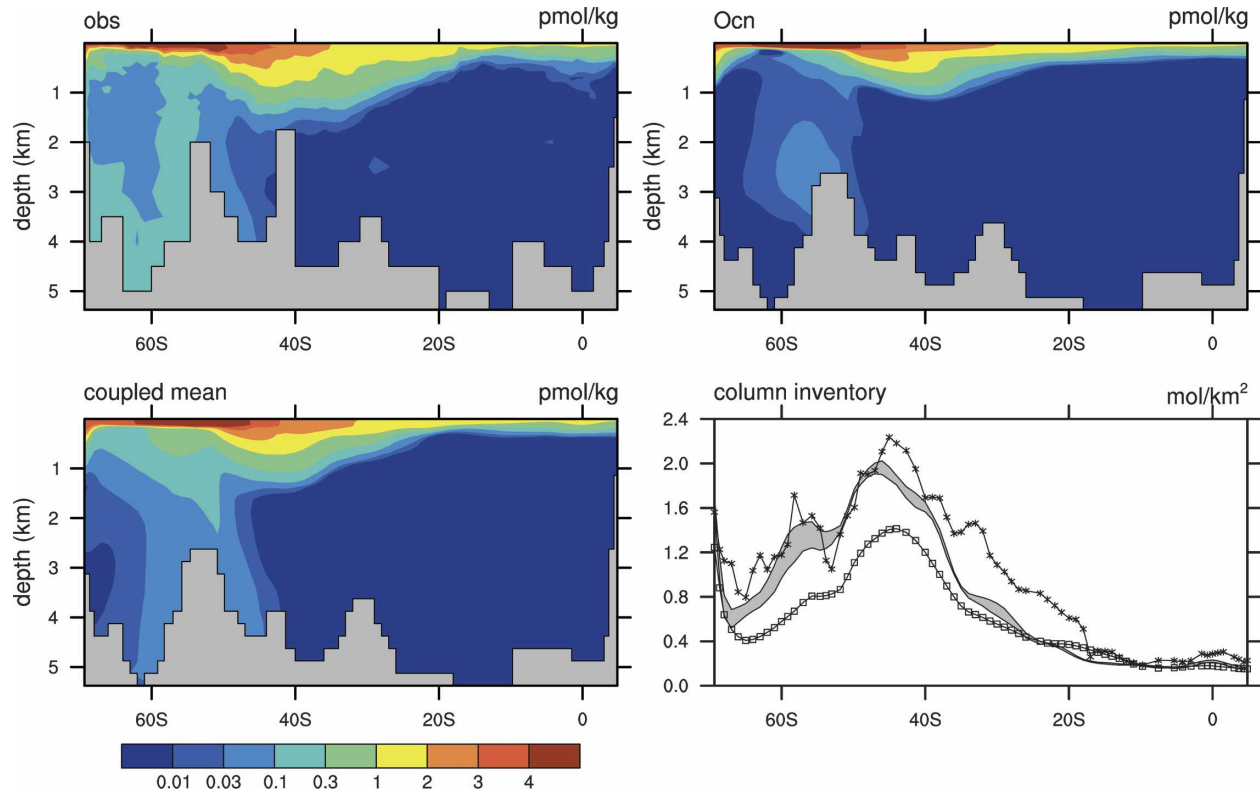


FIG. 2. As in Fig. 1 but from the WOCE AJAX section along 0° taken in October 1983.

semble spread is largest between 50° and 65° S, again where there is significant ventilation of the deep ocean, and the twentieth-century runs match the observations well. The spread is much smaller between 20° and 45° S where the CCSM3 values are significantly smaller than the observations.

Figure 3 shows results from the February 1996 WOCE P14S section near 170° E in the South Pacific. The observations show similar characteristics to the South Atlantic section, with values >1 pmol kg^{-1} down to 1 km between 45° and 55° S and values about 0.1 pmol kg^{-1} in the deep ocean, especially near Antarctica. The subduction along isopycnals is captured quite well by the Ocn and coupled runs, with the higher surface values reaching slightly deeper in the coupled runs. However, there are too high CFC-11 concentrations in the deep ocean in the model at this longitude, and again the twentieth-century runs have higher values than the Ocn run. Figure 3d shows a small ensemble spread along this section, which cannot bracket the much lower observed values near Antarctica at this longitude. This clearly shows that there is too much deep-water formation in the west Pacific sector near Antarctica. The most likely reason is the winds blowing off Antarctica are too strong, which blow the sea ice away

from the coast too quickly. More sea ice is then formed along the coast, which rejects too much brine into the upper ocean and causes more deep convection than in the present climate. Doney and Hecht (2002) show the WOCE P15S section from the CSM1 ocean component alone run forced by observations, where there was too little deep convection at 170° W. They show a strong sensitivity of the convection strength to the salinity values used in the underice restoring term. In an ocean-alone run, this simulates the brine rejection of a fully coupled run, and the deep ocean solutions are sensitive to this restoring term.

Figures 1–3 showed comparisons of CFC-11 concentrations from model simulations with measurements from a single occupation of an ocean section. Differences can arise from other sources than the one we wish to document, which is model systematic bias. The horizontal resolution of the ocean component of climate models, including the CCSM3, does not capture the variability due to mesoscale eddies. Haine and Gray (2001) and Peacock et al. (2005) document the amplitude of eddy variability in CFC-11 concentrations, which they call the model variability error, by using a combination of simulations with eddy-resolving and non-eddy-resolving models. However, in the case of

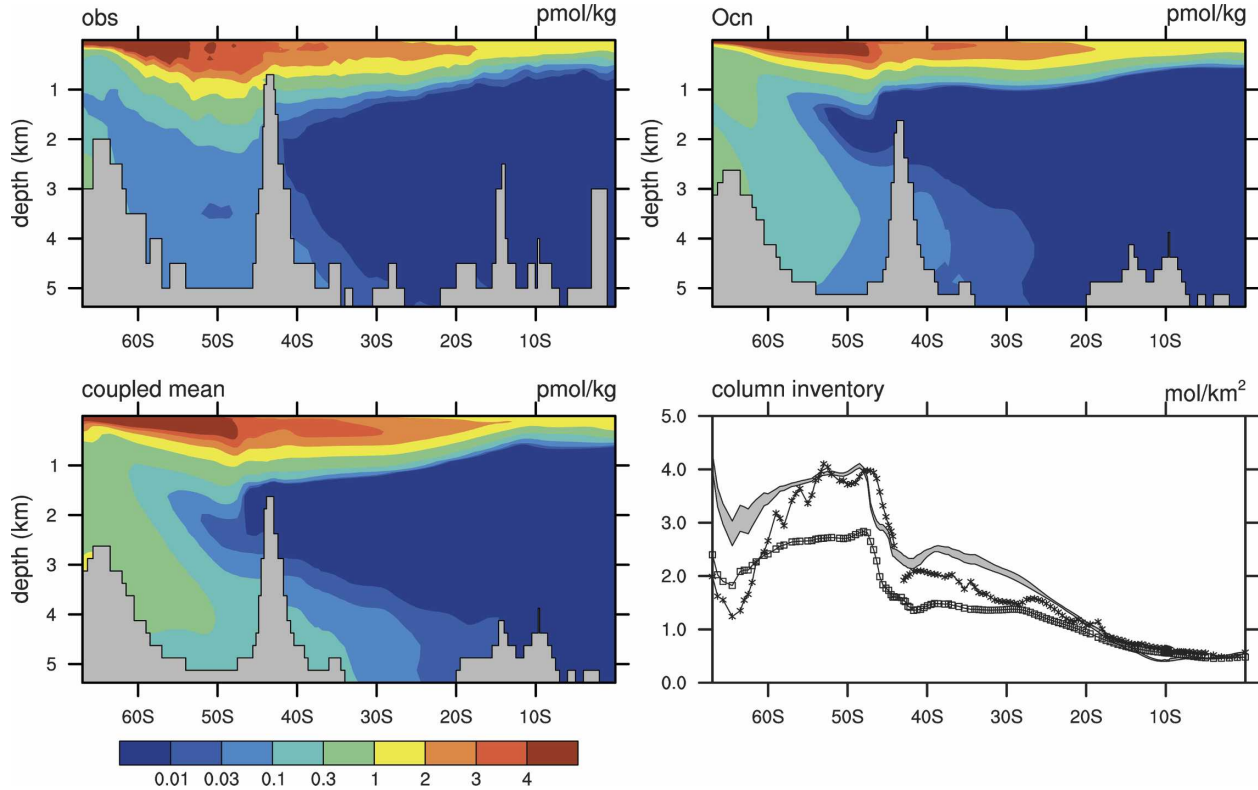


FIG. 3. As Fig. 1 but from the WOCE P14S section near 170°E taken in February 1996.

historical climate simulations, there is another source of disagreement because they are not simulating the state of the climate system for particular years, but rather one of many possible realizations of the climate system for those years. We have attempted to document the amplitude of this realization variability error by showing the ensemble spread in Figs. 1–3, although the ensemble size of three is rather small.

To further document the realization variability error, Fig. 4 shows the root-mean-square of the CFC-11 concentration at 200-m depth in the Indian Ocean relative to the ensemble mean value for each month of 1995. This uses 36 samples (12 months and 3 ensemble members), and is directly comparable with Fig. 7 of Peacock et al. (2005), which shows their model variability error. We note that the realization variability error has a number of features in common with the model variability error. A band of maximum variability runs east–west near 15°S, but with a smaller amplitude compared to the eddy variability shown in Peacock et al. However, the variability among the ensemble members in the Antarctic Circumpolar Current (ACC) region exceeds that due to mesoscale eddies. In contrast, the ensemble has little variability in the Agulhas retroflexion region where mesoscale variability is known to be very large. Background levels of ensemble variability away from

these regions is smaller than the background eddy variability in Peacock et al. Figure 12 of Peacock et al. (2005) shows vertical profiles of CFC-11 at stations along the WOCE i03 track, which document the model

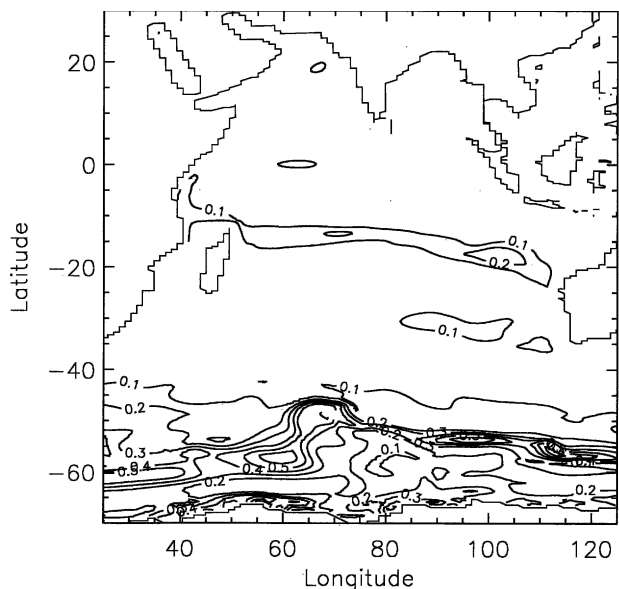


FIG. 4. The rms of CFC-11 relative to the ensemble mean monthly values for 1995 at 200-m depth in the Indian Ocean using the ESb, ESg, and ESh runs; CI is 0.1 pmoles kg^{-1} .

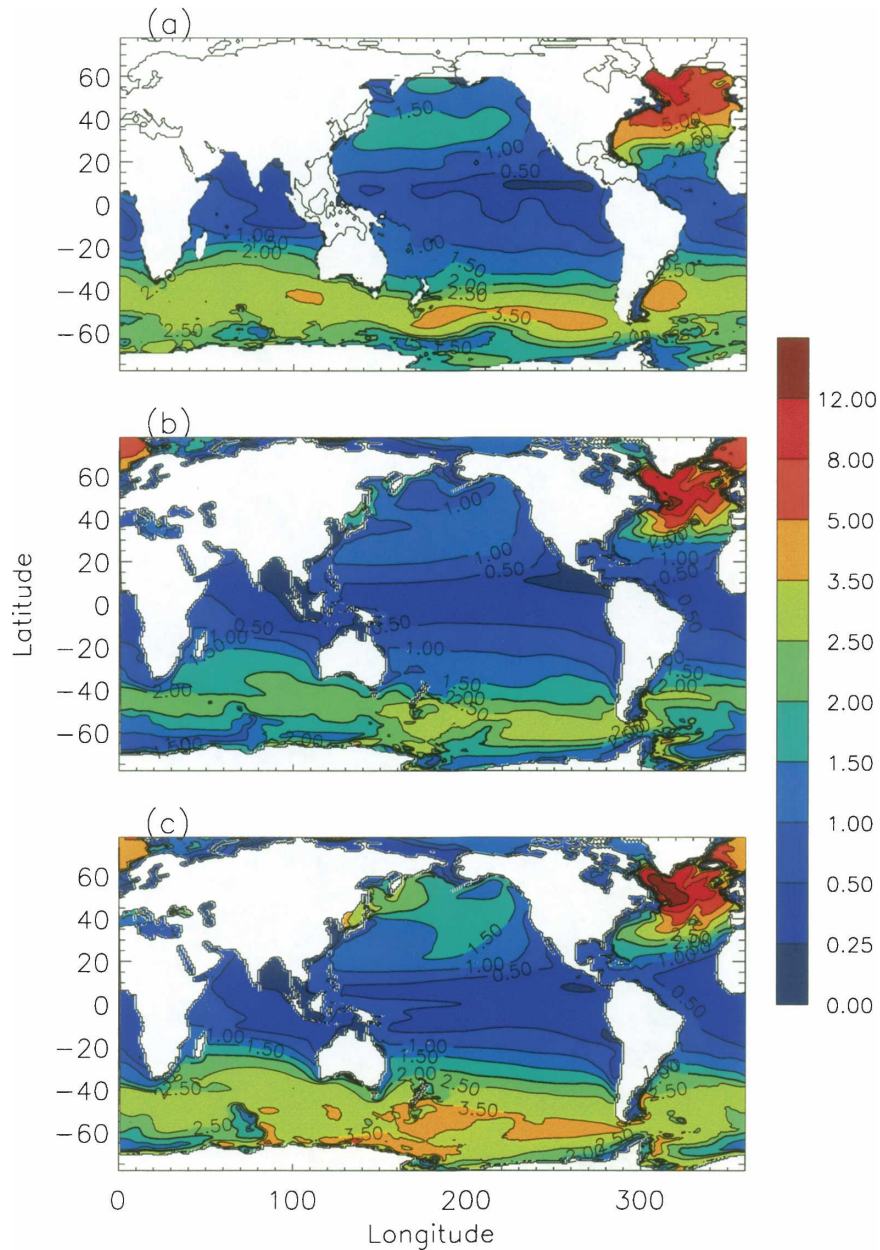


FIG. 5. Column inventory of CFC-11 in moles km^{-2} for 1994: (a) WOCE data from Willey et al. (2004), (b) ocean-alone Ocn run, and (c) mean of ESb, ESg, and ESh runs.

variability error is largest around 400-m depth. The amplitude of the CCSM3 two standard deviation realization variability error of $0.1\text{--}0.2 \text{ pmol kg}^{-2}$ at this depth is an order of magnitude smaller than the model variability error due to mesoscale eddies estimated by Peacock et al.

As mentioned in the introduction, Willey et al. (2004) have produced a column inventory of CFC-11 centered on 1994 from all the WOCE data. It is shown in Fig. 5a, with the same quantity from the Ocn run in Fig. 5b, and

the mean of runs ESb, ESg, and ESh in Fig. 5c. The observations show the smallest values in the Tropics, especially at 10°N in the eastern Pacific Ocean and in the very northern Indian Ocean, and the largest values in the northwest North Atlantic south of Greenland. The other band of large values follows the path of the ACC, and there are smaller values to the south near Antarctica. The Ocn run shows the same general features, but the maximum values are smaller, except in the North Atlantic north of 40°N . As always with

ocean-alone runs, it is rather difficult to know whether the differences compared to observations are due to the forcing data used, in particular to the under ice salt flux used, or to the physics of the ocean component. The twentieth-century runs in Fig. 5c show larger regions of small values in the Tropics, especially in the Pacific where the signature of thermocline depth errors associated with the double intertropical convergence zone shows up clearly. However, at higher latitudes the twentieth-century run values are larger, probably as a result of stronger surface winds that produce deeper ocean mixed layers, stronger midlatitude gyres, and a deeper main thermocline. The values in the ACC are now slightly larger than the observations, but the large values extend to the Antarctic coast in the east Indian and west Pacific sectors. This results from the high values in the deep ocean shown in Fig. 3c along 170°E. This is a region of large discrepancy in the column inventory of CFC-11 between the twentieth-century runs and observations. The values in the northern North Atlantic are also too large, but are not much different than those in the Ocn run.

Another measure of CFC uptake is the penetration depth, which is defined as the column inventory divided by the surface concentration, see Dutay et al. (2002). Figure 6 shows results from observations, the Ocn run, and the twentieth-century run mean in the same format as Fig. 5. In the observations, large values >1 km occur over much of the North Atlantic, with maximum values >2.5 km. In the North Pacific, values up to 900 m occur in the Kuroshio area. In the Southern Hemisphere, values >1 km occur in the southern Indian and Atlantic Oceans and southeast of New Zealand. This pattern is reproduced well in the Ocn run, but the penetration depths are too small, except in the northern North Atlantic. In the twentieth-century runs, the penetration depth is further improved in the North Atlantic, where values >1 km are more extensive and the maximum value is <3 km, and in the southern Indian Ocean and around New Zealand, where the depths have increased by about 200 m compared to the Ocn run. The penetration depth also increased in the North Pacific, but at the southern flank of the subtropical gyre, instead of farther northwest near the Kuroshio.

The variability in the CFC-11 column inventory and penetration depth across the three twentieth century runs is largest by far in the subpolar North Atlantic and the Labrador Sea (not shown). There is smaller variability near Antarctica between 120° and 160°E and off the Kamchatka Peninsula. Elsewhere, the CFC-11 variability is quite small. Much of this variability is caused by the different timing of deep-water formation events in these runs, especially in the North Atlantic.

Figure 7 shows the global CFC-11 inventory as a function of time from the ESb, ESg, ESh, and Ocn runs. There is very little variability in the global CFC uptake rates in the twentieth-century runs, and all have a global inventory of 5.8×10^8 moles in 1994. This compares very well with the Willey et al. (2004) estimate of $5.5 \pm 1.2 \times 10^8$ moles. This very good agreement is not affected by the implementation error described in section 2 because its effect on the global CFC-11 inventory is almost certainly much smaller than the observational error bar of $\pm 20\%$. As discussed above, the Ocn run shows a somewhat smaller global uptake of CFC-11, with a 1994 value just above the lower bound of the estimate based on WOCE observations.

4. Heat uptake results

Levitus et al. (2005) have recently completed a new analysis of heat content changes between 1955 and 2003 over the depth ranges from the surface down to 300 and 700 m and between 1955–59 and 1994–98 from the surface down to 3 km. We will look at heat content changes over these depth ranges in order to compare with the latest Levitus et al. observed trends. Results will be shown in terms of the annual-mean potential temperature for each volume considered. First, this normalizes the heat content with respect to the varying sizes of the different ocean basins and, second, the results are then in terms of familiar temperature units. The average potential temperature can be converted into heat content by multiplying by $\rho_0 c_p$ times the volume of ocean in the various domains. In the model, $\rho_0 c_p$ is constant, equal to $4.1 \times 10^6 \text{ J } ^\circ\text{C}^{-1} \text{ m}^{-3}$.

In the ES1870 run the ocean is losing heat at the globally averaged rate of about 0.5 W m^{-2} over years 300–700. Most of this is coming from middepths in the ocean, but there is a nonnegligible trend in the upper 300 m. To eliminate this small trend, temperature anomalies for both control and ensemble members are calculated by subtracting the linear least squares fit to the ES1870 temperature time series over the period 300–700 yr. The resulting time series of the upper 300-m temperature anomaly from the ES1870 run are shown in Fig. 8. It shows peak-to-peak decadal variability with a maximum range of $>0.2^\circ\text{C}$ in the Pacific Ocean, nearly 0.3°C in the Indian and Atlantic Oceans, and 0.1°C in the global ocean. The Indian and Atlantic Ocean values are comparable to the amplitude of decadal variability shown in Fig. S1 of Levitus et al. (2005); the Pacific Ocean value is a little smaller and the global ocean value is somewhat smaller than the Levitus et al. values. A frequent criticism of coarse-resolution climate models is that they severely underestimate natural

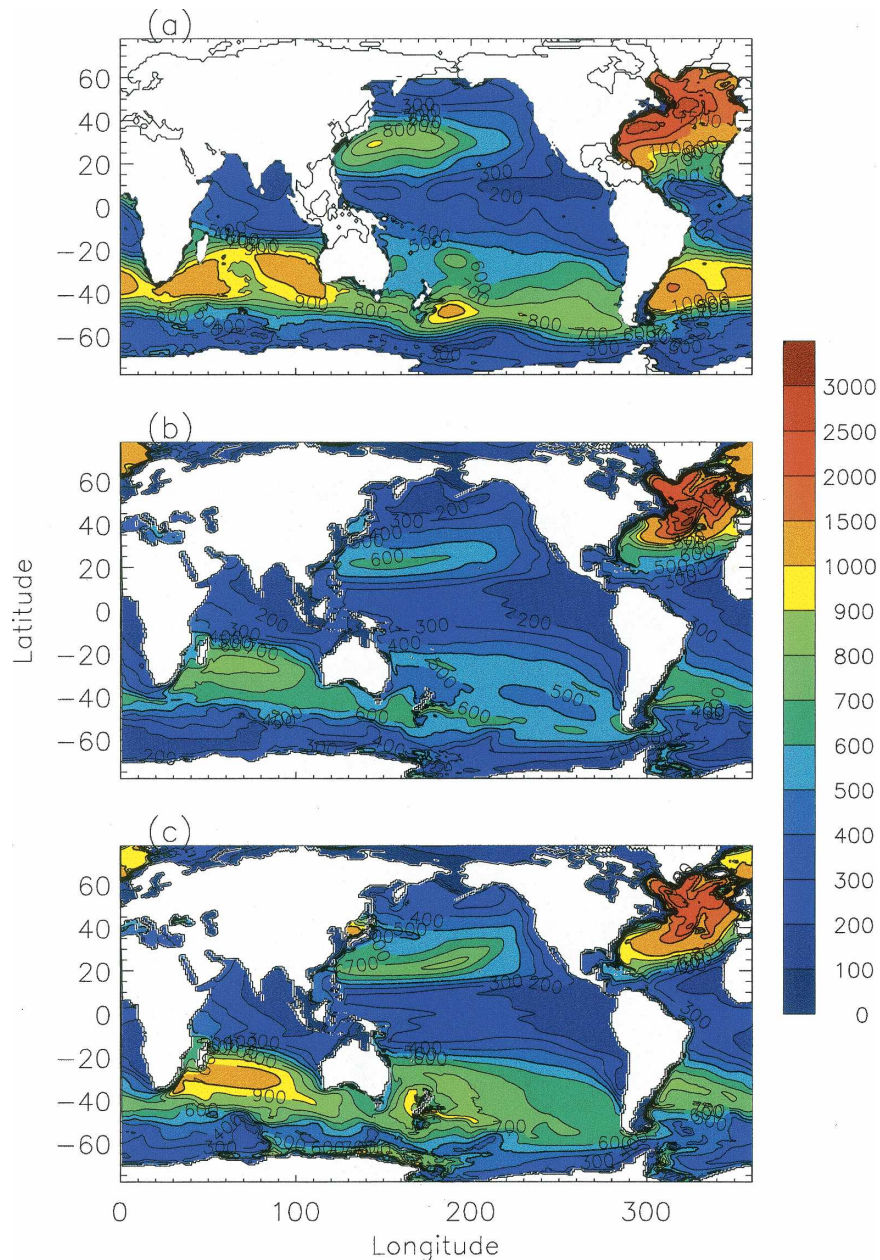


FIG. 6. As in Fig. 5 but for penetration depth in m.

variability; this is not the case for the CCSM3 ocean temperature variability down to 300 m.

Figure 9 shows the average temperature difference down to 300 m between the ESb, ESf, ESg, and ESh runs minus the least squares fit to the ES1870 run trend. Figure 9d shows that the 300-m global ocean temperature either remains nearly constant or falls somewhat over the first 13 yr, but then all four runs have a sharp decline of about 0.1°C in 1883. This is in response to the Krakatoa volcano eruption. In fact, all the six large dips in the curves can be traced to a volcano; the last two are

El Chiçon in 1983 and Mount Pinatubo in 1991. The volcanic signal is also very clear in the Pacific and Indian Oceans, but considerably smaller in the Atlantic Ocean. Even so, the Atlantic loses heat for about 30 yr until 1900 before gaining heat between 1900 and 2000. There is some spread in the rates of ocean heat uptake among the four ensemble members. The ESg run shows much slower heat uptake in the Pacific Ocean between 1940 and 1970, but then it increases so that the heat uptake catches the other three runs by the year 2000. The ESb run shows uniformly more heat uptake in the

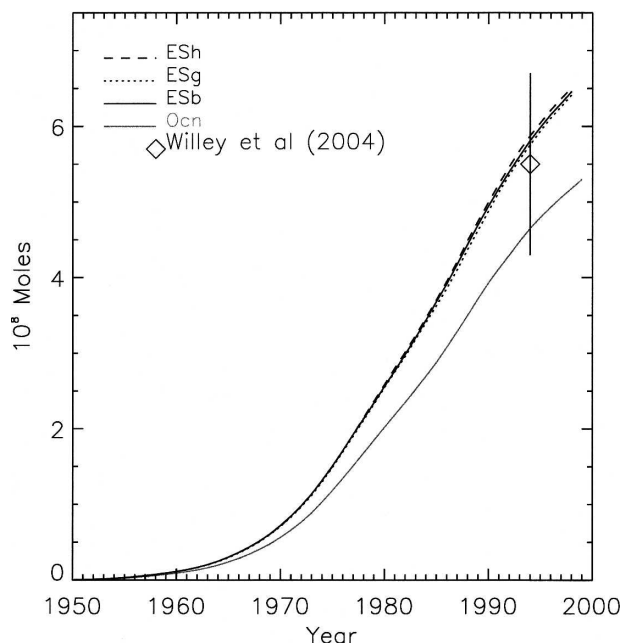


FIG. 7. Time series of the global inventory of CFC-11 in moles from the ESb, ESg, ESh, and Ocn runs. Also plotted is the Willey et al. (2004) estimate centered on 1994.

Indian, Atlantic, and global oceans than the other three runs.

Figure 10 shows the average temperature difference down to 3 km in the same format as Fig. 9. Again, the six large volcano events show up clearly in the global ocean curves. These curves diverge somewhat after 1950, and the ESg run has a 25% larger heat uptake by 2000 than the other three runs. Figure 10c shows very interesting differences in the Atlantic Ocean. By 1970 the ESb run has the same temperature as 1870, whereas the temperature in the ESf and ESg runs has increased by 0.08°C . However, by 2000 there are much smaller differences in the Atlantic temperature among the runs. There are also quite large differences in the Indian Ocean early in the twentieth century and between 1980 and 2000 in the Pacific Ocean, again illustrating significant variability in the ocean circulation among the ensemble of twentieth-century runs.

The global ocean average temperature increases between 1957 and 1996 from the twentieth-century ensemble minus the least squares fit to the ES1870 run trend are plotted in Fig. 11. Also shown are the recent

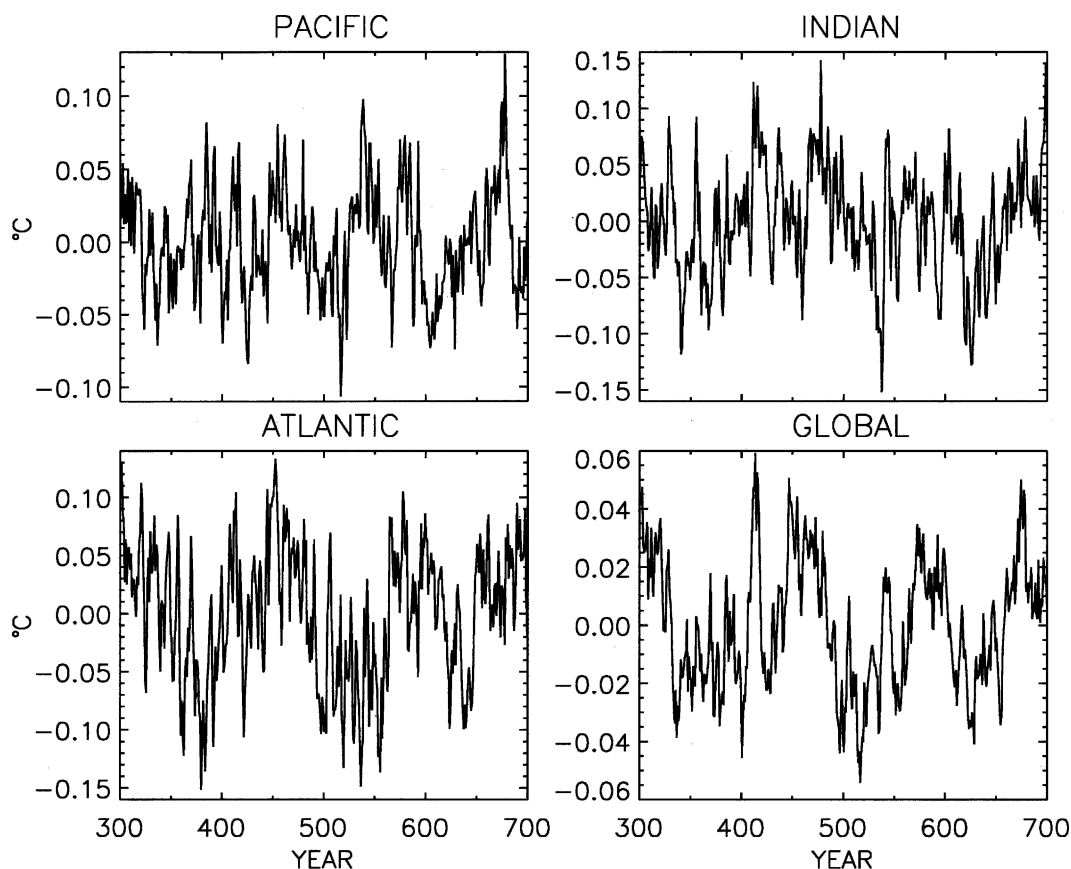


FIG. 8. Detrended time series of the 300-m average temperature anomaly in $^{\circ}\text{C}$ from the ES1870 control run: (a) Pacific Ocean, (b) Indian Ocean, (c) Atlantic Ocean, and (d) global ocean.

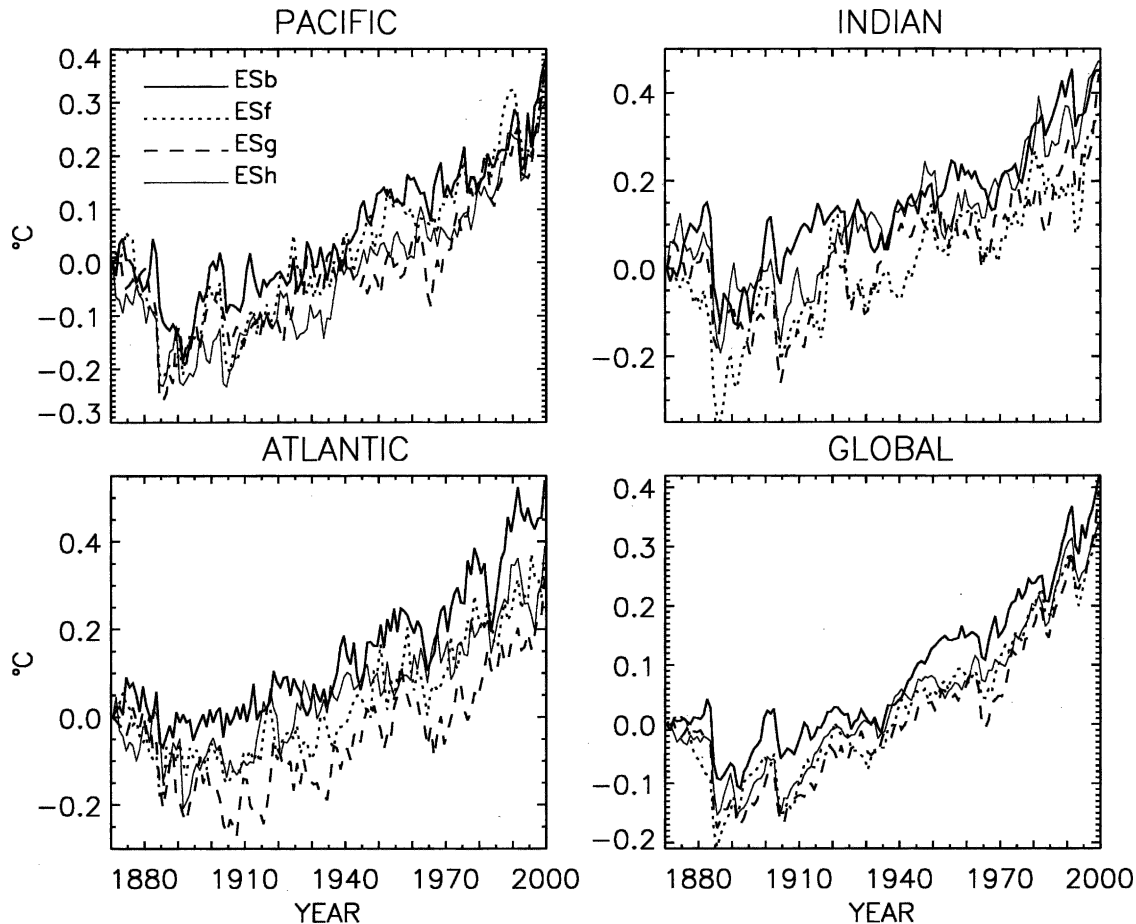


FIG. 9. Time series of the 300-m average temperature difference in $^{\circ}\text{C}$ between the ESb, ESf, ESg, and ESh runs minus the ES1870 control run: (a) Pacific Ocean, (b) Indian Ocean, (c) Atlantic Ocean, and (d) global ocean.

estimates for 300 m, 700 m, and 3 km from Levitus et al. (2005). We should first note that the temperature increases shown are somewhat dependent upon the time interval chosen. The 300-m values would be increased by up to 15% if the time period had been extended to 2000 because the heat uptake is large over the last few years in all runs. Figure 11 shows that the 300-m temperature increase varies by more than a factor of 2 across the ensemble, from 0.12° to 0.267°C . There is considerably less spread in the 700-m temperature increases, which are between 0.116° and 0.19°C , and the ensemble does not bracket the Levitus et al. estimate. This is also the case for the 3-km values, which range between 0.044° and 0.064°C . On average, the ensemble members have about 25% larger temperature change down to 3 km between 1957 and 1996 than the Levitus et al. (2005) estimate from ocean observations.

Figure 12 shows the spatial patterns of the changes in heat content down to 300 m and 3 km between 1955–59 and 1994–98. The heat content has been converted into

a temperature by dividing by $\rho_0 c_p$ times 300 m or 3 km, irrespective of the actual ocean depth. Figure 12a shows that the largest region with an average temperature increase of $>0.4^{\circ}\text{C}$ over 300 m is the subpolar North Atlantic, Labrador Sea, Greenland–Iceland–Norwegian (GIN) Seas, and the Barents Sea north of Norway. There is a dipole structure in the North Pacific, with a significant cooling in the northeast Pacific centered at 40°N . There is also warming in the Southern Hemisphere, with the largest changes probably associated with changes in the path of the ACC. The heat content change down to 3 km, shown in Fig. 12b, is much more spatially uniform, with most of the global ocean warming between 0° and 0.1°C . There are some regions of heat loss in the subtropical North Atlantic, the Southern Hemisphere east of Australia and South Africa, and in the Pacific sector of the Southern Ocean. There is again a large heat content increase in the subpolar North Atlantic, Labrador, GIN, and Barents Seas. This is associated with a retreat of the Arctic sea ice, and

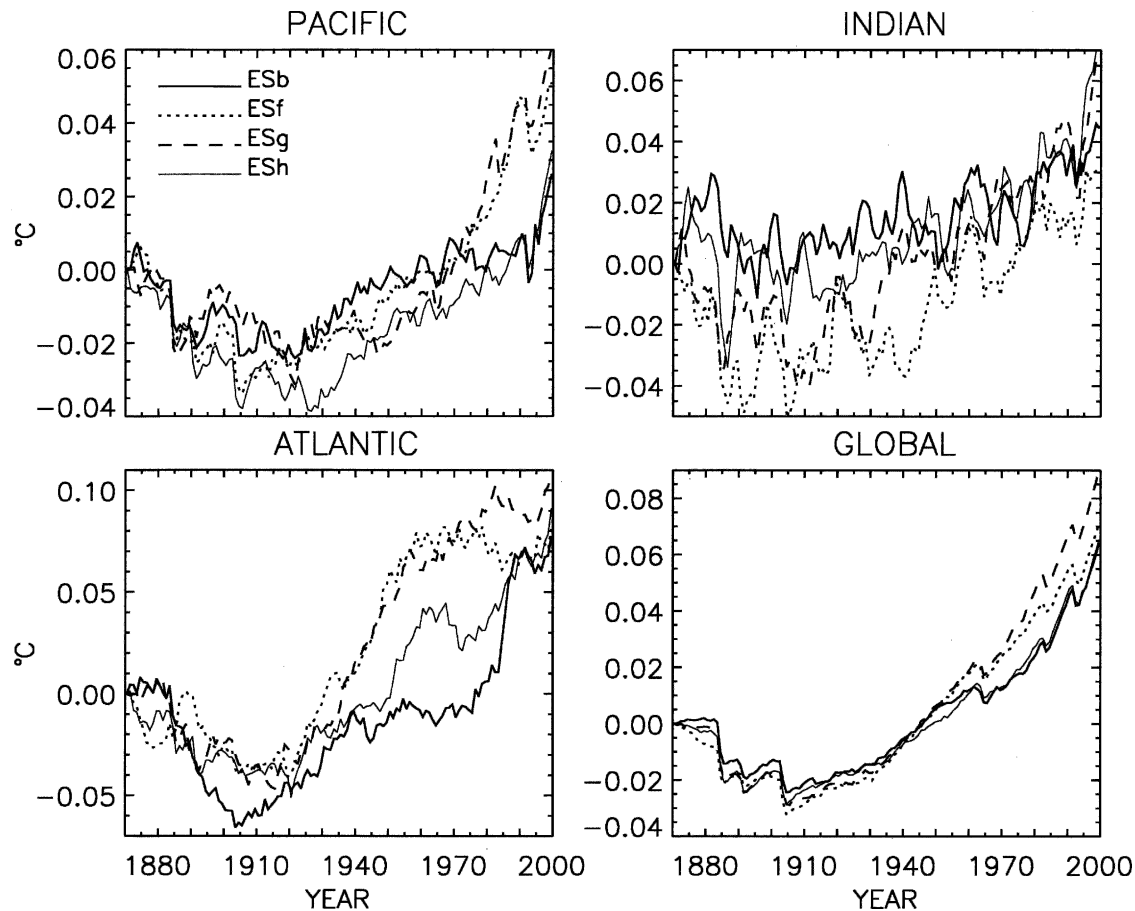


FIG. 10. As in Fig. 9 but for the 3-km average temperature.

perhaps changes in the thermohaline circulation. These large heat content increases are consistent with the Levitus et al. (2005) results since they also find the largest heat content changes in the North Atlantic. They estimate an average temperature increase over 40 yr of 0.3°C down to 300 m and 0.1°C down to 3 km in the North Atlantic, which are at least 50% higher than increases in other large ocean basins. The other area with a large increase in heat content over the second half of the twentieth century is along the path of the ACC in the Southern Ocean.

What causes the wide spread of 300-m heat uptake rates in the twentieth-century ensemble shown in Fig. 11? We will investigate this by comparing the ESh and NCa runs, which have the largest and smallest 300-m temperature changes in Fig. 11. First, the heat content changes between 1955–59 and 1994–98 in the two runs were differenced. This is not shown because the pattern is very similar to the ensemble mean change shown in Fig. 12a, but the amplitude is larger because it is the difference between the two extremes. Similar to Fig. 12a, the difference between the ESh and NCa 300-m

heat uptake patterns is largest in the northern North Atlantic and in the Southern Hemisphere near the ACC.

Figure 13a shows the lag-0 time correlation between the North Atlantic meridional overturning maximum and the 300-m average temperature from the ESh twentieth-century run. We computed a lag-1 autocorrelation of 0.82 from the overturning maximum time series, which indicates that there are about 13 independent samples in the 130-yr time series so that the 95% confidence level is 0.51. The figure shows that the eastern North Atlantic 300-m average temperature is strongly correlated to the maximum value of the overturning circulation. The positive correlation means warmer 300-m temperatures are associated with a stronger overturning circulation. This positive correlation is similar in other twentieth century runs. Figure 13b shows the overturning maximum between 1950 and 2000 from the NCa and ESh runs. The NCa run has the largest range of variability during this period of all the twentieth-century runs, with a range of 10 Sv about a mean of 22 Sv. The strength of the North Atlantic over-

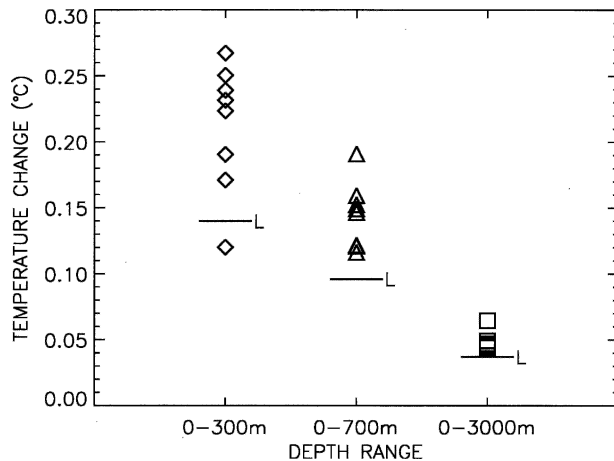


FIG. 11. The 300-m, 700-m, and 3-km average temperature increases in $^{\circ}\text{C}$ for the Global Ocean between 1957 and 1996 from the ensemble of twentieth-century runs. Also plotted are the Levitus et al. (2005) observational estimates.

turning circulation evolves very differently in the two runs. The NCa run has a stronger overturning in 1955–59, resulting in warmer 300-m temperatures, but has a weaker overturning than the ESh run during 1970–2000, resulting in cooler 300-m temperatures when ocean heat uptake is largest. This means that the eastern North Atlantic 300-m temperature change between 1957 and 1996 is much smaller in the NCa run than in the ESh run, which contributes to the spread in Fig. 11.

So, now the question becomes what causes the difference in the maximum value of the meridional overturning? This question is addressed much more fully in Bryan et al. (2006). Their Fig. 1 shows the maximum overturning time series from a control run, where there is an oscillation with a peak-to-peak amplitude of 10 Sv. Thus, the answer is mostly natural variability in the overturning circulation. However, we also note that the variability in heat uptake in twentieth-century runs is influenced by the phase of the meridional overturning oscillation when the run is started. This influence is obviously very strong early in the runs, but is still present even after 80 yr when the runs have reached 1950. The best way to create initial conditions for an ensemble of twentieth-century runs is an interesting and important question, but is beyond the scope of this paper.

We now investigate variability in heat uptake in the Southern Hemisphere by computing the principal components of the sea level pressure field south of 20°S . We use the first principal component as a proxy for the Southern Annular Mode (SAM). Figure 14a shows the lag-0 time correlation between the first principal component coefficient and the 300-m average temperature

from the ESh twentieth-century run. The lag-1 autocorrelation in this case is 0.14, which gives about 99 independent samples in the 130-yr time series so that the 95% confidence level is 0.19. The figure shows the correlation is high along the path of the ACC, with the largest correlation just north of the ACC in the southern Indian Ocean. The SAM and 300-m temperatures are anticorrelated in the southern Indian and Atlantic Oceans, but positively correlated in the southern Pacific Ocean. Again, similar correlation patterns are found in the other twentieth-century runs. Figure 14b shows the time series of the first principal component coefficients between 1950 and 2000 from the NCa and ESh runs. They are very different, and are frequently out of phase, but differ at a higher frequency than the Atlantic overturning time series shown in Fig. 13b. Even so, this demonstrates that the Southern Annular Mode can affect decadal time-scale differences in ocean heat uptake in the vicinity of the ACC path, so its variability can cause some of the spread in the 300-m temperature changes shown in Fig. 11.

5. Discussion and conclusions

The CFC-11 uptake simulations in three twentieth-century runs have been compared with observations from WOCE sections, and are generally good in regions of the ocean where most of the CFC-11 remains above the thermocline. This indicates that the KPP vertical mixing scheme is performing well, and the wind-driven gyre circulations are realistic in these regions. The comparisons show differences where there is deep-water formation in the North Atlantic, and in the west Pacific and Indian Ocean sectors near Antarctica. These differences cannot be explained by the spread in the three twentieth-century runs. An estimate of the realization variability error, due to the fact that these runs do not simulate the climate for particular years, is shown in Fig. 4. A direct comparison with the eddy variability error in Peacock et al. (2005) shows that the eddy error is larger in most regions, but the realization error is larger in the Southern Ocean along the path of the Antarctic Circumpolar Current.

Comparison of individual CFC-11 sections and the model column inventory in Fig. 5 with the observational estimate centered on 1994 in Willey et al. (2004) shows that the CCSM3 is producing too much deep water off Antarctica in the Indian Ocean and west Pacific Ocean sectors. It also suggests the Labrador Sea deep-water formation might be slightly too strong. These aspects of the CCSM3 ocean circulation need to be improved since getting a realistic thermohaline circulation is very important in order that the CCSM3

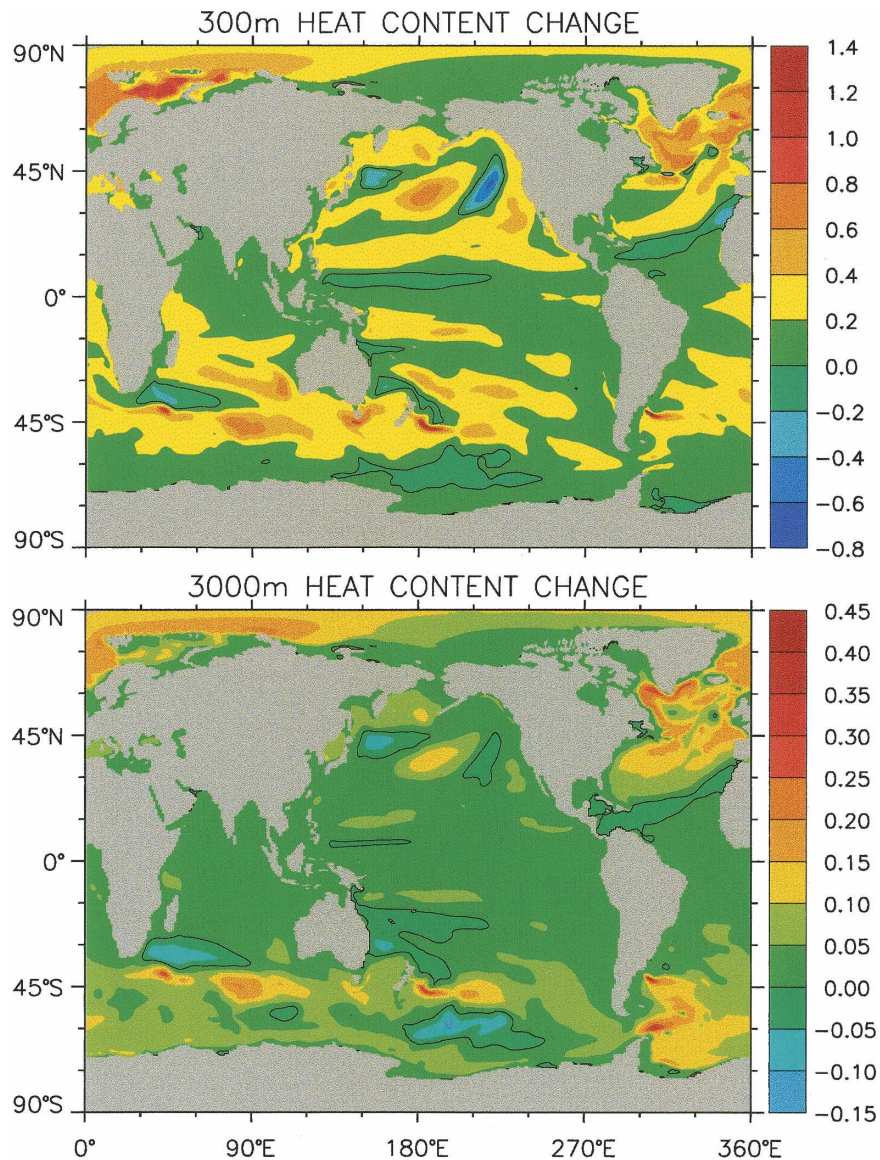


FIG. 12. The ensemble mean twentieth-century average heat content change between 1955–59 and 1994–98 (in $^{\circ}\text{C}$) at (a) 300 m and (b) 3 km.

produces realistic future climate scenarios. Despite these regional differences, Fig. 7 shows the first conclusion of this paper, which is that the global ocean uptake of CFC-11 is captured rather well in the three twentieth-century runs. The CFC-11 uptake in the Ocn run is smaller, but is also within the error bar of the observational estimate.

The way the ocean takes up CFC-11 and heat is not the same. In particular, the strong temperature dependence of CFC solubility introduces a weighting in its uptake to regions of colder surface waters. However, comparing the observed CFC-11 uptake in Fig. 5a and the model heat uptake in Fig. 12b reveals that the areas

of largest uptake are quite similar. If the CCSM3 had done a poor job simulating CFC-11 uptake, then this would have cast considerable doubt on its ability to take up heat correctly. However, CCSM3 does rather well at simulating CFC-11 uptake, and we believe this gives some confidence that heat uptake is also done well.

Figure 8 shows the second conclusion of this paper that the CCSM3 300-m temperature variability is only a little smaller than the Levitus et al. (2005) observational estimate. There is considerable spread in how the ocean takes up heat across the twentieth-century run ensemble. This spread is largest in the 300-m heat up-

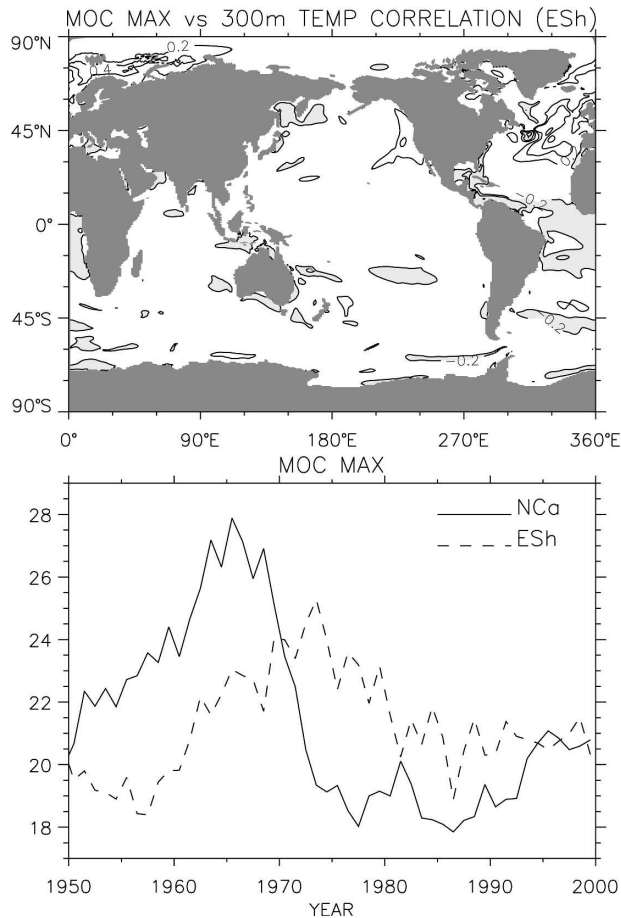


FIG. 13. (a) Correlation between the North Atlantic meridional overturning maximum and the 300-m average temperature for the ESh twentieth century run (CI is 0.2) and (b) time series of the MOC maximum in Sv from the NCa and ESh runs between 1950 and 2000.

take, but occurs across all ocean basins and to all depths. Figure 11 shows that the twentieth-century ensemble spread in 300-m average temperature change between 1957 and 1996 is more than a factor of 2. It decreases with depth, and is about 40% for the 3-km average temperature change. We have documented two causes of this spread in ocean heat uptake. Figures 13 and 14 show strong correlations between the maximum of the overturning circulation and North Atlantic upper-ocean temperature changes and between a proxy for the Southern Annular Mode and temperature changes in the vicinity of the ACC. Thus, variability in the North Atlantic overturning circulation and in the phase of the SAM contribute strongly to the spread in ocean heat uptake across the twentieth-century ensemble.

Figure 11 shows the paper's third conclusion that the ensemble average temperature change between 1957

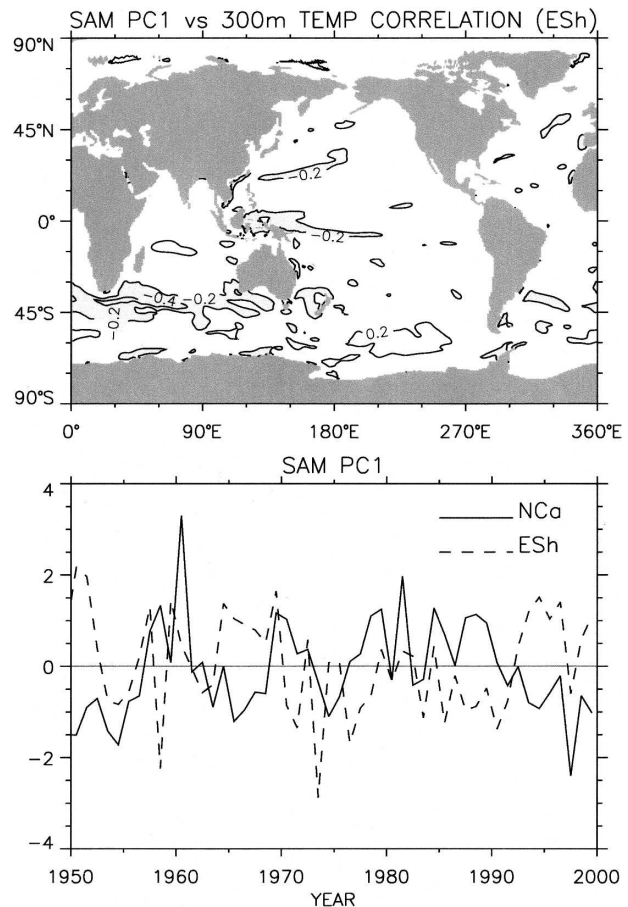


FIG. 14. As in Fig. 13 except using the coefficient of the first principal component of Southern Hemisphere sea level pressure.

and 1996 down to 300 m, 700 m, and 3 km is about 25% larger than the Levitus et al. (2005) observational estimate. There are a number of possible explanations for this, with the first being the intrinsic error in the observational estimate. The second is that the model heat uptake is calculated over the whole ocean, and not just in the regions where there are observations that contribute to the Levitus et al. estimate. Gregory et al. (2004) show this can make a considerable difference to the estimated temperature change. The third is that the CCSM3 has no parameterization of the indirect effects of aerosols. The fourth is that the parameterized effect of volcanoes is not strong enough, although this is very unlikely given the large dips in global ocean temperature shown in Figs. 9 and 10. A fifth is that the rate of heat uptake by the ocean component is too large. However, the successful CFC-11 comparison gives some confidence that the CCSM3 ocean component does a good job simulating the rate of heat uptake into the ocean. The last is that the CCSM3 climate sensitivity of 2.67°C (see Kiehl et al. 2006), is too high. However, the

combined error bar from the first four possibilities is certainly larger than 25% so that we cannot conclude from the ocean temperature change comparison that the rate of ocean heat uptake or the CCSM3 climate sensitivity is incorrect.

Acknowledgments. This study is based on model integrations that were performed by the National Center for Atmospheric Research, and the Central Research Institute of Electric Power Industry, with facilities and support provided by the National Science Foundation, the Department of Energy, the Ministry of Education, Culture, Sports, Science and Technology, and the Earth Simulator Center of the Japan Agency for Marine-Earth Science and Technology. It was made possible by the work of many support staff and scientists at NCAR and CRIEPI.

REFERENCES

- Bitz, C. M., M. M. Holland, M. Eby, and A. J. Weaver, 2001: Simulating the ice-thickness distribution in a coupled climate model. *J. Geophys. Res.*, **106**, 2441–2463.
- Bryan, F. O., G. Danabasoglu, N. Nakashiki, Y. Yoshida, D. H. Kim, J. Tsutsui, and S. C. Doney, 2006: Response of North Atlantic thermohaline circulation and ventilation to increasing carbon dioxide in CCSM3. *J. Climate*, **19**, 2382–2397.
- Danabasoglu, G., W. G. Large, J. J. Tribbia, P. R. Gent, B. P. Briegleb, and J. C. McWilliams, 2006: Diurnal coupling in the tropical oceans of CCSM3. *J. Climate*, **19**, 2347–2365.
- Doney, S. C., and M. W. Hecht, 2002: Antarctic Bottom Water formation and deep-water chlorofluorocarbon distributions in a global ocean climate model. *J. Phys. Oceanogr.*, **32**, 1642–1666.
- , and Coauthors, 2004: Evaluating global ocean carbon models: The importance of realistic physics. *Global Biogeochem. Cycles*, **18**, GB3017, doi:10.1029/2003GB002150.
- Dutay, J. C., and Coauthors, 2002: Evaluation of ocean model ventilation with CFC-11: Comparison of 13 global ocean models. *Ocean Modell.*, **4**, 89–120.
- Gent, P. R., and J. C. McWilliams, 1990: Isopycnal mixing in ocean circulation models. *J. Phys. Oceanogr.*, **20**, 150–155.
- , and G. Danabasoglu, 2004: Heat uptake and the thermohaline circulation in the Community Climate System Model, version 2. *J. Climate*, **17**, 4058–4069.
- Gregory, J. M., H. T. Banks, P. A. Stott, J. A. Lowe, and M. D. Palmer, 2004: Simulated and observed decadal variability in ocean heat content. *Geophys. Res. Lett.*, **31**, L15312, doi:10.1029/2004GL020258.
- Haine, T. W. N., and S. L. Gray, 2001: Quantifying mesoscale variability in ocean transient tracer fields. *J. Geophys. Res.*, **106**, 13 861–13 878.
- Hunke, E. C., and J. K. Dukowicz, 1997: An elastic–viscous–plastic model for sea ice dynamics. *J. Phys. Oceanogr.*, **27**, 1849–1867.
- Kiehl, J. T., C. A. Shields, J. J. Hack, and W. D. Collins, 2006: The climate sensitivity of the Community Climate System Model version 3 (CCSM3). *J. Climate*, **19**, 2584–2596.
- Large, W. G., and S. G. Yeager, 2004: Diurnal to decadal global forcing for ocean and sea-ice models: The data sets and flux climatologies. NCAR Tech. Note, NCAR/TN-460+STR, 111 pp. [Available online at <http://www.cgd.ucar.edu/oce/pubs/04pubs.html>.]
- , J. C. McWilliams, and S. C. Doney, 1994: Oceanic vertical mixing: A review and a model with a nonlocal boundary layer parameterization. *Rev. Geophys.*, **32**, 363–403.
- Levitus, S., J. I. Antonov, T. P. Boyer, and C. Stephens, 2000: Warming of the world ocean. *Science*, **287**, 2225–2229.
- , —, and —, 2005: Warming of the world ocean, 1955–2003. *Geophys. Res. Lett.*, **32**, L02604, doi:10.1029/2004GL021592.
- Meehl, G. A., and Coauthors, 2006: Climate change projections for the twenty-first century and climate change in the CCSM3. *J. Climate*, **19**, 2482–2495.
- Peacock, S., M. Maltrud, and R. Bleck, 2005: Putting models to the data test: A case study using Indian Ocean CFC-11 data. *Ocean Modell.*, **9**, 1–22.
- Raper, S. C. B., J. M. Gregory, and R. J. Stouffer, 2002: The role of climate sensitivity and ocean heat uptake on AOGCM transient temperature response. *J. Climate*, **15**, 124–130.
- Smith, R. D., and J. C. McWilliams, 2003: Anisotropic horizontal viscosity for ocean models. *Ocean Modell.*, **5**, 129–156.
- , and P. R. Gent, 2004: Reference manual for the Parallel Ocean Program (POP): Ocean component of the Community Climate System Model (CCSM2.0 and CCSM3.0). Los Alamos National Laboratory Tech. Rep. LA-UR-02-2484, 75 pp. [Available online at <http://www.ccs.m.ucar.edu/models/ccsm3.0/pop>.]
- Willey, D. A., R. A. Fine, R. E. Sonnerup, J. L. Bullister, W. M. Smethie, and M. J. Warner, 2004: Global oceanic chlorofluorocarbon inventory. *Geophys. Res. Lett.*, **31**, L01303, doi:10.1029/2003GL018816.